Electron emission from small sources

1989 J. Phys.: Condens. Matter 1 9931

(http://iopscience.iop.org/0953-8984/1/49/013)

J. Phys.: Condens. Matter 1 (1989) 9931–9956. Printed in the UK

Electron emission from small sources

N García†‡, J J Sáenz†‡ and H De Raedt§‖

† Departamento Materia Condensada, Universidad Autónoma de Madrid, Cantoblanco, 28049 Madrid, Spain

‡ IBM Research Division, Zürich Research Laboratory, CH-8088 Rüschlikon, Switzerland

§ Physics Department, University of Antwerp, Universiteitsplein 1,B-2610 Wilrijk, Belgium

‖ Natuurkundig Laboratorium, University of Amsterdam, Valckenierstraat 65, 1018 XE Amsterdam, The Netherlands

Received 22 May 1989

Abstract. The development of microtips with controlled geometry at the atomic level has led to the realisation of electron point and teton tip sources. In this work we study the properties of electron emission from microtips of which the size is comparable to the electron wavelength inside the tip and for which quantum effects play an important role in determining the nature of the emitted beam. Numerical integration of the time-independent and time-dependent Schrödinger equation is used to calculate the emitted beam properties such as the energy distribution, the angular width, etc for several models. It is shown that for some particular geometries it is possible to get a significant reduction of the angular width of the emitted beam. We discuss in more detail the electron emission from plane emitting sources, and show that they are particulary well suited to focus the emitted beam. Such electron sources might be very suitable for performing electron holography and interferometry in the reflection mode. Experiments are proposed to test our findings.

1. Introduction

Electron emission from very small sources, i.e. of sources which have a size comparable to the wavelength of the emitted electrons, is a very interesting problem leading to the observation of mesoscopic quantum effects. Recent experimental work on field-emission electrons from point sources [1, 2] and teton tips [3] has demonstrated that the properties of the emitted beams differ markedly from those of beams emitted by conventional sources. The size of these new sources can be made as small as an atom.

An analysis in terms of electron optics [4, 5] shows that at a distance of a few centimetres from the source the electron beam has a transverse (i.e. perpendicular to the direction of propagation) coherence length of a few millimetres. This result is of much relevance for electron holography [6–9] and electron interferometry [10] where large transverse and longitudinal coherence lengths are needed.

Another important feature of these emitted beams is that due to the small dimension of the source, the applied potential needed to get emission is a few hundreds to thousand volts. Consequently these emitted electrons form a low-energy beam which could make them suitable to perform interferometry and holography from surfaces with three-dimensional atomic resolution. In the case of high-energy electrons (10 keV to 400 keV) this is not possible because such experiments are carried out in transmission mode and, as a direct consequence, the phase of the electrons in the longitudinal

0953-8984/89/499931+26$02.50

direction is averaged over the whole electron path. Therefore the resolution of the hologram is good in the transverse direction but very poor in the longitudinal direction [8, 9, 10]. However, if the electron has a low energy then one can perform holography and interferometry in the reflection mode as the electron will penetrate the first few layers only and no averaging of the phase of the electrons takes place.

Another remarkable and important property of these atomic-size sources [1–3] is that the angular spread of the emitted beam is only of a few degrees (smaller than 3°) so that for emission currents of 10^{-9}–10^{-6} A, the source can be quite bright even without using any lenses, provided the source is stable as a function of time. Previous work [4, 5], employing a classical description, has failed to explain the smallness of the angular spread.

Electron emission from small sources can also be obtained by a technique different from field emission of small tips, as has recently been demonstrated by experiments on 2D electron gas (GaAs) systems [11, 12]. By fabricating a device having two reservoirs connected by a narrow constriction, it was shown that the conductance is quantised, the quantisation being a function of the diameter of the constriction. Recent calculations for the conductance of electrons moving from one reservoir via a constriction to another reservoir seem to be in agreement with experiment [13–19].

A similar effect was predicted [20] for the conductance in scanning tunnelling microscope (STM) experiments [21] when the tip and the sample are in the contact regime and the diameter of the contact is varying. As in this particular case the size of the contact is of the order of the wavelength of the electrons, quantum interference effects show up as oscillations in the conductance versus the diameter of the contact. This kind of behaviour appears to have been observed in some STM experiments [22].

All these experiments have in common that the electrons are emerging from some kind of constriction which is of the order of the electron wavelength. The aim of the present paper is to study theoretically various aspects of electron emission from small sources and to examine the properties of the emitted electrons beams. To this end we employ a semiclassical diffraction approximation (SDA) method, and we solve the stationary Schrödinger equation (SSE) and time-dependent Schrödinger equation (TDSE). We will present the energy distribution of the emitted electrons and examine which geometry is best for having a well focused beam. For the case of the GaAs devices our results lead us to propose a technique to focus the current, realisable with present day technology and possibly having interesting technological applications.

The paper is structured as follows. The model as well as the formalisms to solve it are presented in § 2. Section 3 discusses the calculations and numerical results. In § 4 new experiments are proposed to check some of the predictions of our calculations. The conclusions are summarised in § 5.

2. Model and methods

The point source emission experiments [1, 2, 3] are performed on single-crystal (111)-oriented tungsten (W) tips. Determining the band structure and wavefunctions near the tip of such an object is an extremely difficult, unsolved problem at this moment. In order to be able to tackle the problem of point source emission, drastic approximations in describing the metal tip have to be made. As a first step we model the emission tip by a free-electron gas, thereby making the reasonable assumption that the largest contribution to the emitted electrons comes from the s electrons in the metal. Our main

objective is to study general features of the effects of the size and geometric shape of the source on the angular spread and energy distribution of the emitted electrons. The simplest model that captures the basic physics can taken to be two dimensional (2D). In figure 1 we present the geometry of the emitting source in real space together with an energy diagram. Except in the vicinity of the tip, the surface of the source is assumed to be flat. The direction perpendicular (parallel) to the surface (not necessarily the tip as it can have curvature) will be called the longitudinal (transverse) direction.

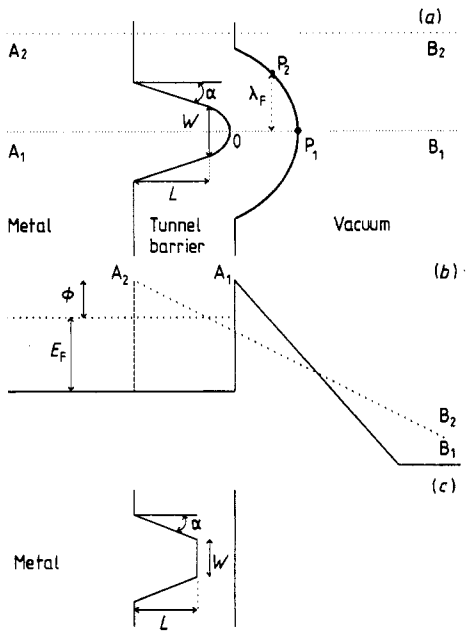

Figure 1. Geometry of the emitting source (*a*) and of the models used in SSE calculations, the corresponding energy diagram (*b*) and the geometry of the plane emitting source (*c*).

Figure 1(*a*) shows that the tip is characterised by the width W, the length L, the angle α and a given geometrical shape, i.e. hyperbolic, elliptical or plane (figure 1(*c*)). The metal–vacuum interface consists of a tunnel barrier of a given shape depending on the tip geometry and the applied electric field $\boldsymbol{F}$. Figure 1(*b*) depicts the energy scheme corresponding to the geometry of figure 1(*a*). The two parameters characterising the free-electron gas are the Fermi energy E_F (or wavelength λ_F) and the work function ϕ. Figure 1(*c*) shows a particular case of figure 1(*a*) that we will call plane emitting source (PES). We will pay special attention to this geometry as our calculations show that from the point of view of focusing the beam it has remarkable properties.

Another important reason to study the PES of figure 1(*c*) is that for $\alpha \simeq 0$, and small values of the tip width W, the presence of well separated energy levels in the transverse direction may lead to drastic changes in behaviour. It has been shown experimentally and theoretically† that the conductance through a constriction connecting two reservoirs at the same Fermi energy is quantised. It is an open question

† Notice that in the experiments [11, 12] and in the theoretical work [13–19] the constriction connects to reservoirs and there is no tunnel barrier. The current distribution has an angular spread of approximately 60°.

to what extent the level quantisation will affect the properties of the emitted electron waves and if it does so, whether the focusing of the beam is governed by the geometry of tip, the tunnel barrier or both.

Assuming that the electrons inside the metal can be modelled by a free-electron gas, the total intensity of emitted electrons can be written as

$$I = \frac{e}{\pi\hbar} \int \mathrm{d}E \sum_i T_i(E) \tag{2.1}$$

where E is the total electron energy and the summation runs over all angles of incidence θ_i. The transmission probability $T_i(E)$ for an angle of incidence θ_i can be written as

$$T_i(E) = \sum_j T_{j,i}(E) \tag{2.2}$$

where the sum over j runs over all possible outgoing angles θ_j. According to (2.1) and (2.2) the transmitted intensity can be calculated once all the $T_{j,i}$ are known. In the following sections we compute the $T_{j,i}$ following three different recipes.

2.1. Semiclassical diffraction approximation

To study the problem of electron emission from small sources, we have to deal with a very complicated quantum mechanical problem, which can only be solved by application of more or less sophisticated scattering methods. It is of interest to compare these scattering calculations with the results of a simple semiclassical model. Although, the results of the latter are only qualitative, it will give insight into the importance of the different model parameters involved.

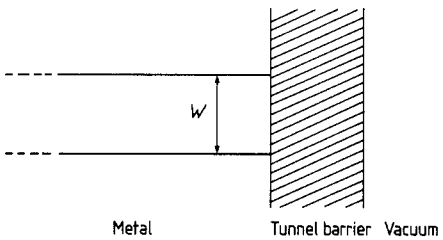

Figure 2. Geometry of the model used in SDA calculations.

For simplicity we will restrict the discussion to 2D systems having a flat tunnelling barrier, i.e. a PES. The geometry of the model we want the study is that of figure 2, for a semi-infinite constriction. In this case electron energy is fully quantised and given by

$$E(q_x, n) = \frac{\hbar^2}{2m}\left[\left(\frac{n\pi}{W}\right)^2 + q_x^2\right] \tag{2.3}$$

where q_x is the longitudinal wavevector of the electron, n is the quantum number that determines the wavevector $q_n = n\pi/W$ in the transverse direction, m is the effective electron mass that will be taken as equal to the electron mass (unless we are discussing the 2D electron gas in GaAs devices).

In this case (2.1) reads

$$I = \frac{e}{\pi\hbar} \sum_{n=1}^{N_{\max}} \int_0^{E_F} T_n(E)\, dE \tag{2.4a}$$

where the sum runs over all quantised levels and

$$N_{\max} = \text{Int}\left[W\sqrt{2mE_F}/\pi\hbar\right]. \tag{2.4b}$$

Note that if only electrons at the Fermi level contribute to the current, (2.4) leads to the approximate quantum conductance formula for narrow constrictions

$$\sigma = \frac{e^2}{\pi\hbar} \sum_{n=1}^{N_{\max}} T_n(E_F). \tag{2.5}$$

Assuming that there is no diffraction on entering of the barrier, the tunnel probability is given by

$$T_n(E) = T\left(E - \frac{\hbar^2}{2m}\left(\frac{n\pi}{W}\right)^2\right)\Theta\left(E - \frac{\hbar^2}{2m}\left(\frac{n\pi}{W}\right)^2\right) \tag{2.6}$$

where as usual $\Theta(x)$ is the Heaviside step function, and we have adopted the expression of transmission through a 1D barrier, which depends on the longitudinal energy

$$E_x = E - \frac{\hbar^2}{2m}\left(\frac{n\pi}{W}\right)^2 \tag{2.7}$$

only. For simplicity $T(E_x)$ is taken to be the WKB expression

$$T(E_x) = \exp\left[-4k_F s(\phi + E_F - E_x)^{3/2}/3\phi\sqrt{E_F}\right] \tag{2.8}$$

where s is the distance a plane wave having wavevector $q_x = k_F$ ($k_F = 2\pi/\lambda_F = \sqrt{2mE_F}/\hbar$) has to travel through the triangular barrier. Results obtained from an exact numerical solution of the 1D problem merely differ quantitatively.

One of the most important properties of the electron beams is the energy spread of the total current. Within our simple model the longitudinal current (normal energy) distribution of the emitted electrons is given by

$$J_N(E_x) \equiv \frac{e}{\pi\hbar}\text{Int}\left[\frac{W\sqrt{2m(E_F - E_x)}}{\pi\hbar}\right] T(E_x). \tag{2.9}$$

whereas the total energy distribution is given by

$$J_T(E) = \frac{e}{\pi\hbar} \sum_{n=1}^{N_{\max}} T_n(E). \tag{2.10}$$

Although the energy distribution $J_T(E)$ does not reveal the quantisation effect due to the small size of the source, the quantum levels might still have some influence

on the angular distribution of the emitted current. To analyse the angular spread of the current, we now take into account the scattering of electrons at the end of the constriction. As a first approximation to this problem, we will envisage each scattered plane wave to be filtered incoherently by the tunnelling barrier, i.e. we will assume that the transmittance of a given electron having a total energy E and transverse momentum $q_n = n\pi/W$ is given by

$$T_n(E) \simeq \int_{-1}^{+1} |f_n(q \sin\theta)|^2 T\left(\frac{\hbar^2 q^2 \cos^2\theta}{2m}\right) \mathrm{d}(\sin\theta) \tag{2.11}$$

where $f_n(q \sin\theta)$ is the diffraction function of the constriction or, in other words, the Fourier transform of the slit function. The total current can now be written as

$$I \simeq \int_{-\pi/2}^{\pi/2} I(\theta) \cos\theta \, \mathrm{d}\theta \tag{2.12a}$$

whereby

$$I(\theta) \equiv \frac{e}{\pi\hbar} \sum_{n=1}^{N_{\max}} \int_0^{E_F} |f_n(q \sin\theta)|^2 T\left(\frac{\hbar^2 q^2 \cos^2\theta}{2m}\right) \mathrm{d}E. \tag{2.12b}$$

In this approximation each electron leaving the constriction is scattered, and each of the scattered waves goes into the tunnelling barrier, with a momentum $q_x = q\cos\theta$, normal to the barrier. Although this is a very rough approximation to the problem, it may give us a qualitative picture of the physics involved.

2.2. Exact solution to the stationary Schrödinger equation

As pointed out above, the angular spread and energy distribution of the current directly follow from the knowledge of the $T_{j,i}(E)$. To calculate $T_{j,i}(E)$ we use the 'matching scattering technique' which has proven itself in STM [23, 24], quantum resistances of interfaces [25], and point contacts [13]. It consists of matching the wavefunction in the metal, i.e. a linear superposition of plane waves (incident plus reflected waves), with the appropriate linear combination of waves in the tunnel barrier and with a linear superposition of waves in the vacuum region, taking into account the changes in energy due to the applied field. The appropriate wavefunctions for the square tunnel barrier are exponentials, whereas for the triangular tunnel barrier they are Airy functions. For each electron moving in the direction of the tip, the matching is done at the points A_1, A_2 and B_1, B_2 (see figure 1), using a grid of points fine enough that the unitarity condition, that is the sum of all transmittivities plus all reflectivities equal to one [23–25], is satisfied. Each electron impinging on the surface is described by a plane wave having an angle of incidence θ_i. The outgoing, transmitted, waves are also plane waves having a scattering angle θ_j and a corresponding transmittivity $T_{j,i}(E)$. From the latter quantity all interesting properties such as the angular spread and the energy distribution follow directly.

2.3. Exact solution to the time-dependent Schrödinger equation

The formalisms developed in the previous two sections relied on the basic assumption that the waves incident on the barrier can be thought of as being (incoherent combinations of) plane waves. In this section we concentrate on the situation where that is

not the case. The electron wave that is emitted from an atomic-size source may behave like a wavepacket, i.e. as a particular linear combination of plane waves. Under such circumstances investigation of the emitted-beam properties requires the solution of the time-dependent Schrödinger equation (TDSE).

The basic idea is to solve the TDSE

$$i\hbar\frac{\partial\psi(\boldsymbol{r},t)}{\partial t} = H\psi(\boldsymbol{r},t) \tag{2.13}$$

for a quantum particle that moves towards the constriction, tunnels through a potential barrier and then proceeds to move in vacuum, under the influence of a slowly varying (in space) external field. The geometry of the problem is that of figure 3. The Hamiltonian H takes the form

$$H = \frac{\hbar^2}{2m}p^2 + V(\boldsymbol{r}) \tag{2.14}$$

where $V(\boldsymbol{r}) = 0$ if $\boldsymbol{r}$ is inside the source (including the constriction), $V(\boldsymbol{r}) = \infty$ at the source boundary except at the exit plane of the constriction, and for all $\boldsymbol{r}$ outside the source, $V(\boldsymbol{r})$ is determined by the particular geometry of the tip (i.e. plane triangular, elliptical, etc) and field chosen.

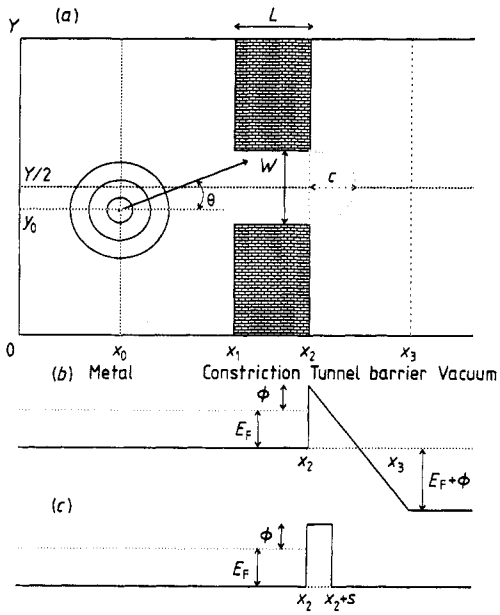

Figure 3. Geometry of the models used in TDSE calculations (*a*), and the energy diagrams for the triangular (*b*) and rectangular (*c*) barrier respectively.

For reasons of computational economy it is necessary to introduce dimensionless variables. In all our TDSE calculations the length scale is expressed in units of λ_F, wavenumbers are measured in units of $k_F = 2\pi/\lambda_F$, energies in units of $E_F = \hbar^2 k_F/2m$, and times in units of $\hbar/E_F$. The corresponding TDSE and Hamiltonian read

$$\frac{\partial\psi(\boldsymbol{r},t)}{\partial t} = -iH\psi(\boldsymbol{r},t) \tag{2.15a}$$

and

$$H = -\frac{\nabla^2}{(2\pi)^2} + \frac{V(\boldsymbol{r})}{E_F} \tag{2.15b}$$

respectively.

The computer simulation consists of preparing a wavepacket and letting the wavepacket evolve in time according to the TDSE (see figure 3). The TDSE is solved numerically by means of an algorithm based on a fourth-order Trotter formula [26]. Propagation of the wave is considered entirely in real space, i.e. without involving Fourier transformations. The method is unconditionally stable and very efficient, allowing the solution of problems sufficiently 'large' to be physically meaningful.

A convenient choice for the initial wavepacket is a Gaussian of width κ moving towards the constriction with wavevector $\boldsymbol{q}$. In the reduced units introduced above, the expression for a Gaussian packet, moving in free space, reads

$$\Phi(\boldsymbol{r},t) = \pi^{-d/4}\kappa^{d/2}(\kappa^2 + \mathrm{i}t/2\pi^2)^{-d/2} \exp\left(2\pi\mathrm{i}\boldsymbol{q}\cdot\boldsymbol{r} - \mathrm{i}q^2t^2 - \frac{(\boldsymbol{r}-\boldsymbol{q}t/\pi)^2}{2(\kappa^2+\mathrm{i}t/2\pi^2)}\right) \tag{2.16}$$

where d denotes the dimensionality of space (in most of our TDSE calculations $d = 2$). The initial state is then simply $\Phi(\boldsymbol{r}-\boldsymbol{r}_0, t=0)$ whereby $\boldsymbol{r}_0$ denotes the position of the centre at $t = 0$. By varying $\boldsymbol{r}_0$ or the angle $\theta_i = \tan^{-1}(q_y/q_x)$ we can simulate different situations as far as the approach of the packet to the constriction is concerned.

After (part of) the wavepacket has travelled through the constriction and has tunnelled through the potential barrier (if present), a Fourier transform with respect to the spatial coordinates of the transmitted wavepacket $\tilde{\psi}(\boldsymbol{r},t)$ is carried out. Here and in the following the tilde indicates that the transmitted packet has been separated from the rest of the wavefunction. The resulting probability distribution

$$|\tilde{\psi}(\boldsymbol{q},t)|^2 \propto \left|\int \mathrm{d}\boldsymbol{r}\, \exp(2\pi\mathrm{i}\boldsymbol{q}\cdot\boldsymbol{r})\, \tilde{\psi}(\boldsymbol{r},t)\right|^2 \tag{2.17}$$

more clearly reveals the main properties of the outgoing wave than the corresponding real-space intensity.

We close this section with some technical remarks about the simulations themselves. To approximate the continuum model, use has been made of the standard three- and five-point difference approximation to the second derivative with respect to the coordinate. The mesh size was chosen such that the length scale λ_F corresponds to 20 grid points. This ensures that the discretisation itself is sufficiently accurate. The time step was chosen such that the results were independent of it, up to four significant digits. As the program used [26] was not written for this particular application, memory requirements effectively limited the number of lattice points in the simulation box to about 415 000. Most of the 2D simulations were carried out using a box of $40\lambda_F \times 13\lambda_F$. Occasionally artefacts due to the relatively short length of the vacuum region (see figure 3(*a*)) in the longitudinal direction have been observed. Work to reduce the memory usage of the code by a factor of 2 is in progress. A typical 2D simulation takes 20 minutes of CPU time on a (2-pipe) CYBER 205 and 7 times longer on an IBM 3090–300E/VF.

3. Results

In general our calculations show that the focusing of the beam is most effective for PES, i.e. when the tip resembles a plane source (geometry of figure 1(*c*)). This conclusion is drawn from comparison of results for different geometries and is in agreement with earlier, semiclassical calculations [13] for the hyperboloid, ellipsoid and paraboloid tips that showed that the angular spread at the source was approximately 20–30°, followed by a field focusing in the region of space where the electrons propagate in the applied field. This focusing reduces the angular spread by a factor of about 2, for an applied field of a few hundred volts. Therefore the angular spread at the screen obtained in [5] is 10° to 15°, much larger than the $\approx 5°$ observed experimentally [1–3].

3.1. SDA calculations

Although not a genuine scattering calculation, the SDA helps us to assess the importance of the different mechanisms involved. Figure 4 shows the distribution of electrons emitted from a tube without a tunnel barrier (or, in other words, for a very large field) as obtained in the SDA. The calculations presented are for $W = 10$, 20, 30, 60 Å and $E_F = 8$ eV ($\lambda_F = 4.4$ Å). The normalised intensity distribution as well as the intensity corresponding to each of the quantum modes of the tube are shown. The main conclusion is that the width of the intensity profile (angular spread) is practically independent of the width W and approximately 120°. Figure 4 clearly shows that decreasing the dimension of the tip does not lead to any focusing.

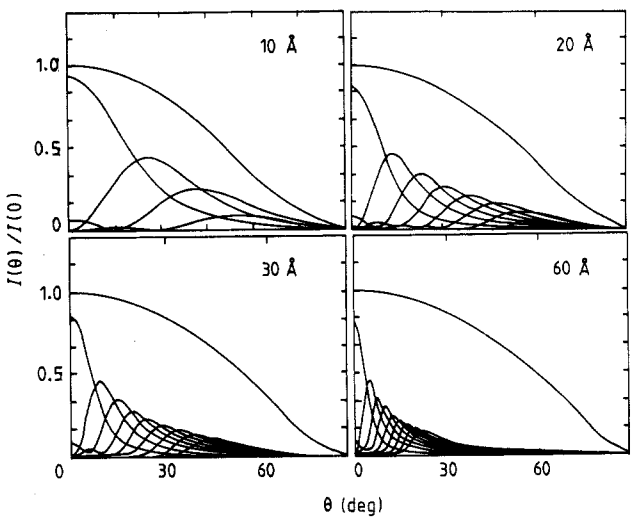

Figure 4. Angular distribution of the emitted current $I(\theta)$ for the case without a tunnelling barrier and for the values of W shown. Also shown are contributions of the first few energy levels of the source. SDA calculation.

In figure 5 we show the energy spectra (see (2.10)) at zero temperature of the emitted current for constrictions of different width, followed by a triangular barrier with a constant field $F = 0.5$ V Å^{-1} and a Fermi energy and work function of 8 eV and 4.5 eV respectively. As it can be seen, the normal energy distribution $J_N(E_x)$ clearly reflects the level quantisation of the source, showing peaks corresponding to

the energy levels present in the source. However, the total energy distribution $J_T(E)$ is an almost constant function, independent of the constriction width W, i.e. $J_T(E)$ is mainly determined by the filtering effect of the tunnelling barrier. The relatively narrow peak in the energy spectra comes from the triangular shape of the tunnelling barrier. Of course, the width in energy ΔE ($\Delta E \simeq 0.3$ eV in the present case) decreases with decreasing field.

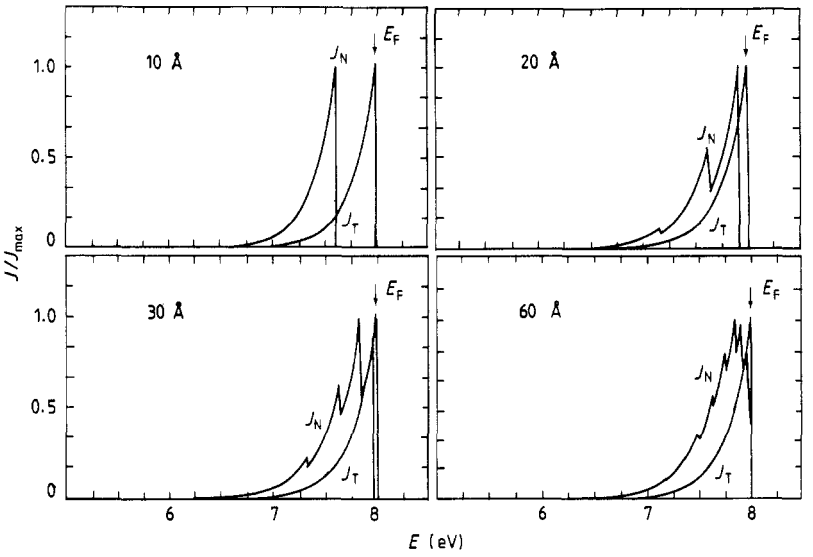

Figure 5. Total (J_T) and normal (J_N) energy distribution of the current emitted from a planar source for the different sizes of W shown, for a 2D electron gas with a Fermi energy $E_F = 8$ eV and a work function $\phi = 4.5$ eV. The tunnelling barrier is assumed to be triangular with a field $F = 0.5$ V Å^{-1}. SDA calculation.

The results shown in figure 5 suggest that from an energy analysis of the emitted current only, experimental observation of level quantisation would be difficult unless one is able to discriminate between longitudinal and total energy.

In figure 6 the current density as a function of the outgoing angle θ, for different widths W, has been plotted. Also shown in figure 6 are the contributions of the first two levels of the source ($n = 1, 2$). From figure 7 it can be seen the angular spread of the beam, measured as the half angle at half intensity, is approximately constant as a function of the constriction width W, this in spite of the fact that the relative importance of the various contributions clearly changes with W. For small W, the emitted current consists mainly of electrons coming from only one level, yielding a wave which, in this case, has an angular spread of $\Delta\theta \simeq 10°$ at the emitting surface.

For wide constrictions (W large), a different picture emerges. In this case, diffraction effects are very weak, and each electron wave having a momentum q has an angular width $\Delta\theta_q$ which is very small. However, the current density now is given by the *non*-coherent sum of a large number of electrons coming from different levels. In the end, the total current has an angular spread $\Delta\theta \simeq 10°$ which is much larger than that of the individual electron waves.

The results discussed above can be understood as follows. Because of the filtering effect of the triangular barrier, only those electrons having energies close to the Fermi

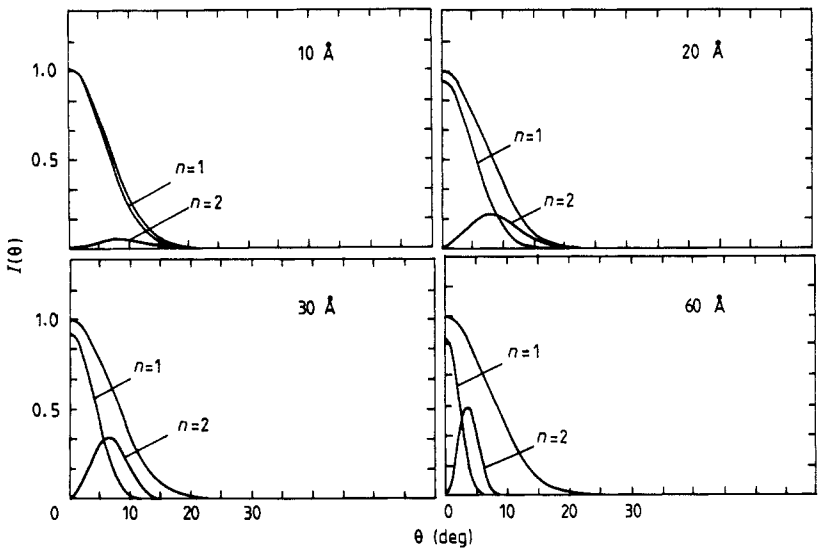

Figure 6. Angular distribution of the emitted current $I(\theta)$ for the same parameters as in the previous figure. Also shown are curves corresponding to the contribution of the first ($n = 1$) and second ($n = 2$) energy levels of the source. The angular width at half intensity remains approximately constant ($\approx 10°$) and is independent of the source width W, whereas the angular width of the contribution of each level becomes smaller as W increases. SDA calculation.

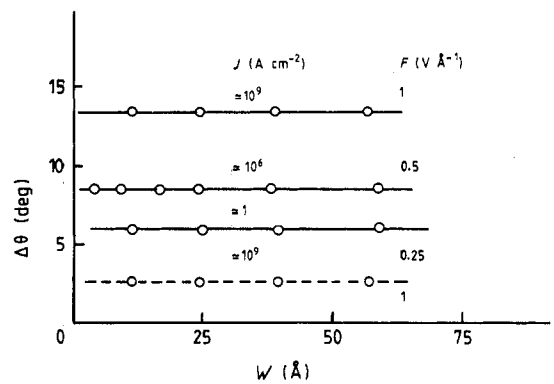

Figure 7. Angular spread of the emitted current, as a function of the source size W, for applied fields $F = 0.25$, 0.5 and 1.0 V Å^{-1}. Broken line: angular spread obtained by incorporating the field reduction for planar geometry [4, 5] for an applied potential of 200 V. SDA calculation.

energy E_F will contribute significantly to the total current. Then, we can write

$$I(\theta_{out}) \simeq \frac{e}{\pi\hbar} \sum_{n=1}^{N_{max}} |f_n(k_F \sin\theta_{out})|^2 \, T\left(\frac{\hbar^2 k_F^2 \cos^2\theta_{out}}{2m}\right) \tag{3.1}$$

where θ_{out} denotes the angle of the outgoing wave with respect to the longitudinal direction. For narrow constrictions (W small), $N_{max} = 1$ and the diffraction function $|f_n(k_F \sin\theta_{out})|^2$ is a smooth function of the angle θ_{out}. As the transmission probability

decays exponentially, the angular width will be determined by the tunnelling properties of the barrier. The angular width, defined as the angle at which the intensity drops by a factor of two compared to the intensity in the longitudinal situation, is then obtained from the solution of the simple equation

$$T\left(\frac{\hbar^2 k_F^2 \cos^2 \Delta\theta}{2m}\right) = 1/2. \tag{3.2}$$

For large W, the diffraction function approaches a delta function

$$|f_n(k_F \sin \theta_{out})|^2 \propto \delta(\theta_{in} - \theta_{out}) \tag{3.3}$$

where θ_{in} is the angle of the incident wave, i.e. $\tan \theta_{in} = n\pi/qW$. As before the angular spread is controlled by $T(k_F \cos \theta_{in}) \simeq T(k_F \cos \theta_{out}) \simeq 1/2$ leading to the same angular spreading of the electron beam, but as argued before, due to a different physical mechanism.

The fact that in the SDA the waves are being diffracted before they penetrate the barrier not only affects the angular spread but also modifies the longitudinal current distribution, simply because the tunnelling barrier favours incident waves which are normal to the barrier. This focusing effect results in a shift of the energy distribution towards higher longitudinal energies E_x (i.e. towards directions closer to the normal to the barrier).

3.2. SSE calculations

All SSE calculations are done for for a geometry in which $\alpha = 45°$ (see figure 1(*c*)). This ensures that the results have converged as a function of the number of plane waves employed in the numerical solution. Calculations were performed using the same values of E_F and ϕ as in the SDA case.

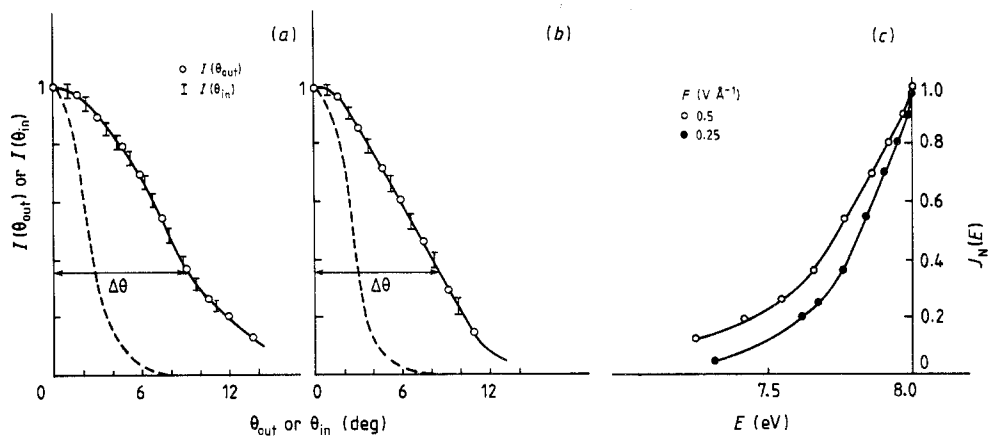

Figure 8. Angular distribution of electrons emitted from a PES: (*a*) $W = 2\lambda_F$, (*b*) $W = 4\lambda_F$ and $F = 0.25$ V Å^{-1} for both cases. See text for more explanation about $I(\theta_{out})$ and $I(\theta_{in})$. Broken curve: angular spread obtained by incorporating the field reduction, adopting the same parameters as in the previous figure. Also shown (*c*) is the energy distribution of the emitted wave for $F = 0.25$ and 0.5 V Å^{-1} respectively. SSE calculation.

In concert with the SDA results we find an angular spread of approximately 60° when no tunnel barrier is present, a result which is independent of the value of W for the range of parameters of interest and in agreement with the TDSE calculation (see next section). SSE calculations for the PES geometries (figure 8) and the SDA results are comparable. The angular spread $\Delta\theta \simeq 9°$ and $\Delta\theta = 11°$ for applied fields of $F = 0.25$ V Å^{-1} and $F = 0.5$ V Å^{-1} respectively. When we take instead of a triangular barrier, a square barrier having the same value of ϕ and a thickness of 6 Å, the angular spread increases. The SSE calculations also show that the angular spread is practically independent of the width W of the emitting tip. Figure 8(c) shows the energy distribution of the current for the two values of F mentioned previously. It is seen that the smaller the field is, the smaller is the energy spread. The angular spread of the beam for the elliptical tip and a field of $F = 0.5$ V Å^{-1} at the apex of the tip is about 25° showing that the beam is focused very little by the barrier. Also in this case the angular spread is independent of W (see figure 9).

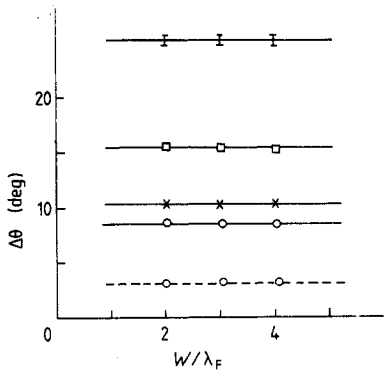

Figure 9. Angular spread, obtained from plots shown in the previous figure but now as a function of W. Bars: elliptical tip and square barrier; open squares: PES, square barrier ($\phi = 4.5$ eV, $s = 5$ Å); crosses: PES, triangular barrier, $F = 0.5$ V Å^{-1}; open circles: PES, triangular barrier, $F = 0.25$ V Å^{-1}; broken line: PES, triangular barrier, $F = 0.5$ V Å^{-1} incorporating the same field reduction as in figure 7. SSE calculation.

A physical interpretation for this behaviour can be given by noting that for the curved geometries the equipotential lines follow the shape of the tip. We find that in order to focus the emitted electrons, the geometry of the tunnel barrier has to satisfy

$$\exp[-(s_1 - s_2)\sqrt{\phi}] < 1/e \tag{3.4a}$$

or, equivalently

$$\sqrt{\phi} > (s_1 - s_2)^{-1} \tag{3.4b}$$

where s_1 and s_2 are the distances between the points O–P_1 and O–P_2, P_1 and P_2 being a Fermi wavelength λ_F apart (see figure 1). Notice that the points P_1 and P_2 are on the equipotential line to obtain a given current. Equation (3.4) is easy to interpret from the physical point of view. It implies that the thickness of the tunnel barrier has to be increased by $\phi^{-1/2}$ for two points of the equipotential surface separated by a distance λ_F. For realistic values of E_F, ϕ and F, the PES satisfies the criterion discussed above

and nicely focuses the emitted electrons. For the elliptical tip, condition (3.4) is not satisfied and therefore the electrons spread over a large angle.

An interesting observation is that if we plot the current summed over all outgoing angles as a function of the incoming angle (i.e. $I(\theta_{in}) \equiv \sum_{\theta_{out}} I(\theta_{in}, \theta_{out})$) or the current summed over all ingoing angles as a function of the outgoing angle (i.e. $I(\theta_{out}) \equiv \sum_{\theta_{in}} I(\theta_{in}, \theta_{out})$) we find the same result. This is illustrated in figure 8 where the bars indicate the transmitted intensity as a function of the incident angle. We believe that this result holds to a good approximation in the case where the incident wave is a plane wave.

A summary of the angular spreads obtained from SSE calculations for different geometries and tunnel barriers is presented in figure 9. Our conclusion is that of all the geometries considered, the PES yields the best focusing. Equivalently one might say that in the direction normal to the emitting plane, the tunnel distance is shorter. Consequently a smaller angle of incidence yields a larger transmittivity. Note that as the barrier is a very effective filter for low-energy electrons (lower part of figure 8), only the electrons with energies between E_F and $E_F - \Delta E$ contribute significantly to the current. The angular width for PES

$$\Delta\theta = \cos^{-1}([(E_F - \Delta E)/E_F]^{1/2}) \simeq (\Delta E/E_F)^{1/2} \tag{3.5}$$

for $\Delta E = 0.3$eV is in good agreement with the SSE calculations.

We emphasise that our SSE calculations are in excellent agreement with the SDA results, showing that the latter is an excellent approximation. The picture that emerges is then that the waves are first diffracted at the end of the constriction representing the tip, without focusing effects due to quantised levels in the constriction, and are subsequently filtered in energy and direction by the tunnel barrier. This filtering is the most effective for triangular barriers and especially for the PES.

3.3. TDSE calculations

Figures 10 and 11 depict typical simulation results for $|\tilde{\psi}(\boldsymbol{r}, t)|^2$ and $|\tilde{\psi}(\boldsymbol{q}, t)|^2$ for the case without and with a plane triangular barrier with $\phi = 0.5E_F$ and $x_3 - x_2 = 10\lambda_F$ (see figure 3) respectively. In the absence of a potential (figure 10) the width of $|\tilde{\psi}(\boldsymbol{q}, t)|^2$ as a function of q_y, i.e. in the direction perpendicular to the direction of propagation q_x, is rather large indicating that there is a lot of diffraction and that the angular spread $\Delta\theta$ is large. In the case shown, the transmitted intensity $T(\theta_i = 0°) \simeq 0.6$, assuming the probability of the incident wave is normalised to one, as usual. Turning on the potential leads to significant changes in $|\tilde{\psi}(\boldsymbol{q}, t)|^2$ as is most evident by comparing figures 10 and 11. The width in q_y is much smaller now. As expected on general grounds, the transmitted intensity, which is about 3×10^{-3} in this particular case, is much lower than in the case without the potential.

Simulation data for $|\tilde{\psi}(\boldsymbol{q}, t)|^2$ for the same plane triangular barrier as in figure 11, but for a constriction of $L = \lambda_F/2$, are depicted in figure 12. The shape and the width of $|\tilde{\psi}(\boldsymbol{q}, t)|^2$ in both directions is within numerical accuracy the same as in the former case, as is the transmittivity. This is a direct consequence of working with idealised, uniform (in the y direction) potentials. From figure 3 it follows that the wavepacket will hit the potential barrier at an earlier instant if the constriction is made shorter (x_1 is kept fixed in all our simulations) so that the emitted wave will leave the barrier earlier too. Hence the shorter the constriction is, the longer the emitted wave will be subject to the accelerating field. From the real-space pictures it seems reasonable to

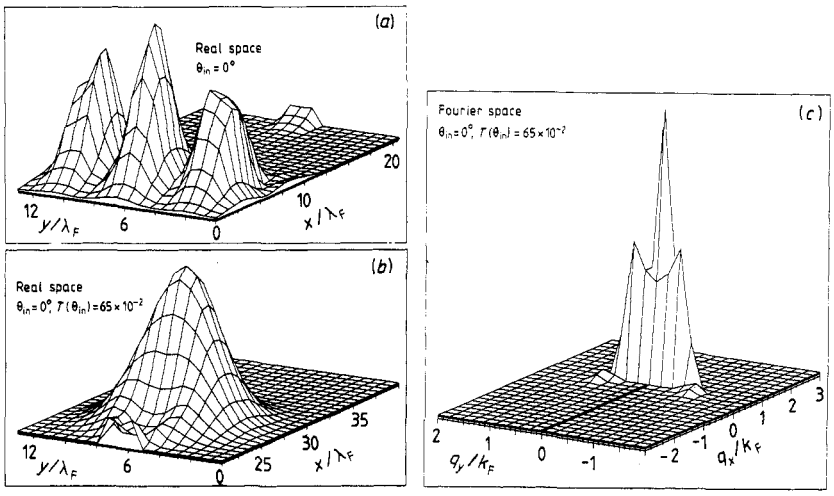

Figure 10. (*a*) Probability distribution of the reflected wavepacket. The constriction has a length $L = 5\lambda_F$ and a width $W = 2\lambda_F$, and the width of the initial Gaussian wavepacket $\kappa = 1.5$ (in units of λ_F). (*b*) Probability distribution of the transmitted wavepacket. (*c*) Intensity in q-space, obtained by Fourier transforming the outgoing wavepacket. TDSE calculation.

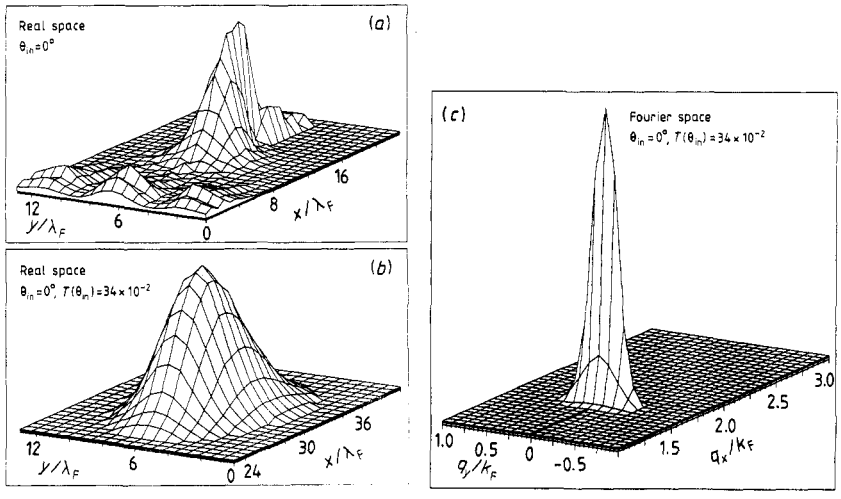

Figure 11. (*a*), (*b*) and (*c*) Same as in the previous figure except that in addition to the constriction a plane triangular barrier is present.

assume that for the times t considered, the transmitted wavepacket can be looked upon as being separated from the rest of the wave and moving in a constant external field. Then a rigorous calculation yields

$$\left|\tilde{\psi}\left(q_x + \frac{E_0\tau}{E_F}, q_y, t_0 + \tau\right)\right|^2 = |\tilde{\psi}(q_x, q_y, t_0)|^2 \tag{3.6}$$

showing that the only effect of the field E_0 is to displace $|\tilde{\psi}(\boldsymbol{q}, t)|^2$ by an amount $E_0\tau/E_F$ along the q_x direction. Thus, under the hypothesis that the transmitted packet is a

separate entity, acceleration due to the constant external field does not alter the shape of $|\tilde{\psi}(\boldsymbol{q},t)|^2$.

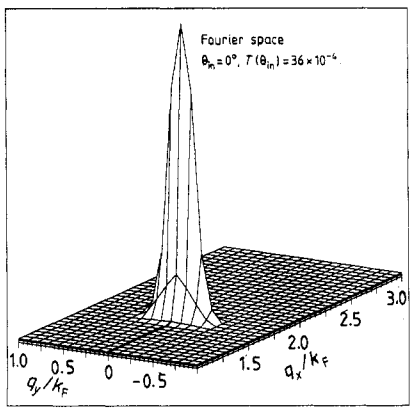

Figure 12. The Fourier-transformed transmitted wave $|\tilde{\psi}(\boldsymbol{q},t)|^2$ emerging from a constriction of $L = \lambda_F/2$ followed by a plane triangular barrier. TDSE calculation.

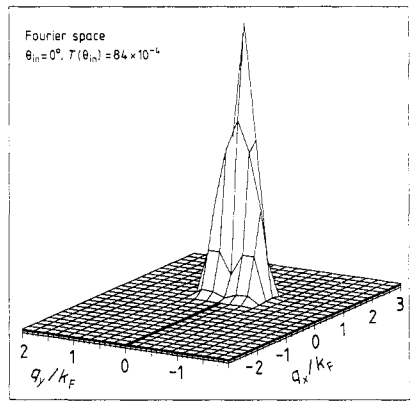

Figure 13. The Fourier-transformed transmitted wave $|\tilde{\psi}(\boldsymbol{q},t)|^2$ emitted by an elliptically shaped tip. Constriction: $L = \lambda_F$. TDSE calculation.

Extensive calculations have shown that changing the length L of the constriction has no significant effect on $|\tilde{\psi}(\boldsymbol{q},t)|^2$ in the case where a tunnel barrier is present. Without potential the diffracted wave is of course changing quantitatively as L is varied ($\lambda_F/2 \leq L \leq 5\lambda_F$ in our simulations) but, most importantly, the width of the profile in the q_y direction is only weakly depending on L. However, in the case when a tunnel barrier is present, our results do not reveal any dependence of $|\tilde{\psi}(\boldsymbol{q},t)|^2$ on the length L. Summarising, without a potential barrier the scattering is sensitive to the length of the constriction whereas in the case with a triangular barrier no such effects are seen.

To illustrate that the PES is a very efficient filter that focuses the beam in the longitudinal direction, figure 13 shows a typical result for $|\tilde{\psi}(\boldsymbol{q},t)|^2$ for the case of an elliptical tip ($W = 2\lambda_F$, $c = 3\lambda_F$, see figure 3). Although the potential was chosen such that the distance through the barrier, for an incident plane wave of energy E_F, is identical to that of the PES ($\approx 1.67\lambda_F$), the transmittivity of the former is more than a factor of two larger than that of the latter. From figure 13 it is clear that the extra intensity is not only going into the longitudinal components of the packet but adds considerably to those with $q_y \neq 0$ as well. We conclude from this that the elliptical tip does not focus as well as the PES, a conclusion we believe holds for tips of other curvature too.

All these conclusions about the behaviour of $|\tilde{\psi}(\boldsymbol{q},t)|^2$ are drawn from calculations in which the initial packet is symmetric with respect to the axis passing through the centre of the constriction. To assess the quality of the tunnelling barrier as a focusing device it is necessary to investigate what happens for the case of non-normal incidence, i.e. at $t = 0$, $\theta_i \neq 0$ and $y_0 \neq Y/2$. In general $|\tilde{\psi}(\boldsymbol{q},t)|^2$ is asymmetric in q_y, the shift of the maximum of $|\tilde{\psi}(\boldsymbol{q},t)|^2$ with respect to $q_y = 0$ being much smaller than the width of $|\tilde{\psi}(\boldsymbol{q},t)|^2$ in the q_y direction. Note the big difference between the peak positions of $|\tilde{\psi}(\boldsymbol{q},t)|^2$ for the case without (figure 14(*c*)) and with a plane triangular barrier

(figure 15(*c*)). It is obvious that the plane triangular barrier has very good focusing properties. In concert with our earlier finding for the case of normal incidence, our simulation results (not shown) reveal that the elliptically shaped tip does not perform as well.

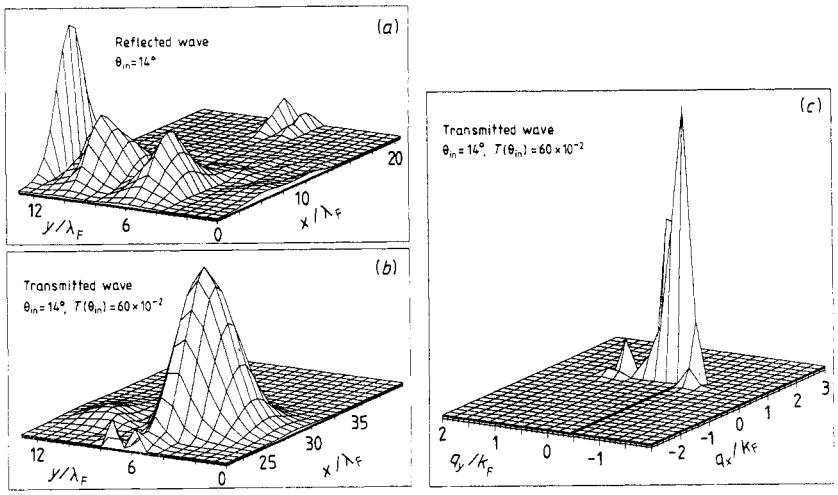

Figure 14. Intensities in real (*a*) and (*b*) and Fourier space (*c*) for non-normal incidence. The constriction has a length $L = 5\lambda_F$ and a width $W = 2\lambda_F$, and the width of the initial Gaussian wavepacket $\kappa = 1.5$ (in units of λ_F). The angle of incidence with respect to the direction normal to the surface is 14°. No potential barrier is present. The thick line indicates the q_y component at which the Fourier-transformed wavefunction reaches its maximum. TDSE calculation.

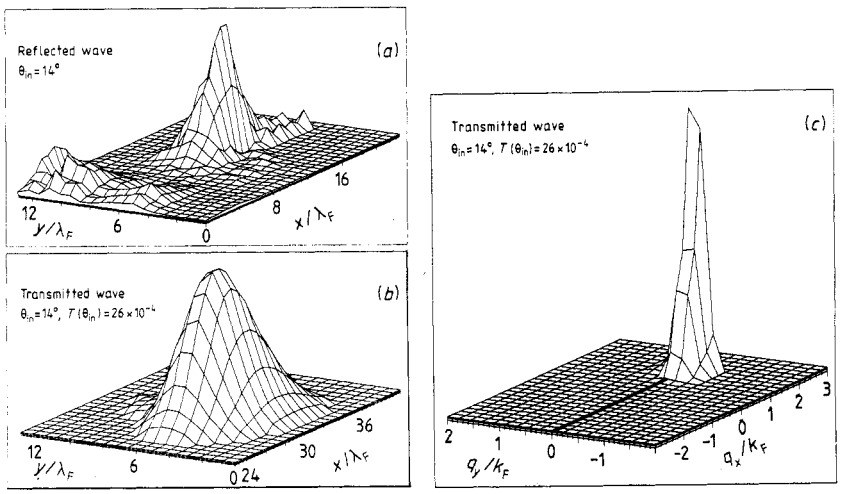

Figure 15. (*a*), (*b*) and (*c*) Same as in the previous figure except that in addition to the constriction a plane triangular barrier is present.

Our PES simulation data yield angular spread $\Delta\theta \simeq 5°$. Converting the model parameters used in the TDSE calculations gives a field of $F = 0.55$ eV Å^{-1}. Comparison

with the SDA (figure 7) and SSE (figure 9) results shows that the TDSE approach predicts a smaller angular spread, i.e. focusing is better than expected on the basis of SDA and SSE calculations. Notice that in this case there is an extra field focusing the emitted electrons due to the potential used (see figure 3).

Anticipating the optical transmission experiments to be proposed in §4, we also performed a set of simulations for the case of a constriction followed by a rectangular barrier (see figure 3(*c*)). The distance d was chosen such that a wave, having incident energy E_F, sees a barrier of the same thickness as it would have seen if a triangular barrier were present. Again it is important to examine the focusing properties by sending to the barrier wavepackets with different angles of incidence. One of the resulting plots of $|\tilde{\psi}(q,t)|^2$ is given in figure 16. In contrast to the plane triangular-barrier case, $|\tilde{\psi}(q,t)|^2$ has much more structure now. Two peaks, one with $q_y < 0$ and one with $q_y > 0$, are clearly visible. On the other hand, the transmittivity relative to the transmittivity for normal incidence is about a factor of two less than for the triangular barrier. Thus, although for non-normal incidence ($\theta_i \neq 0$), $|\tilde{\psi}(q,t)|^2$ has more structure than in the case of the triangular barrier, the total transmitted intensity is much less.

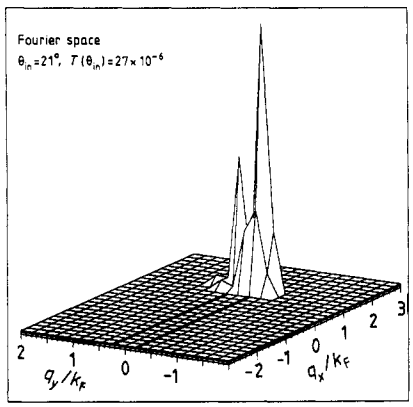

Figure 16. The Fourier-transformed transmitted wave $|\tilde{\psi}(q,t)|^2$ of a source consisting of a constriction ($L = 5\lambda_F$) followed by a plane rectangular barrier of $W = 1.667\lambda_F$ for a non-normal incident wavepacket. TDSE calculation.

We can understand this behaviour by means of SDA-like arguments, by considering one of the plane waves contributing to the incident wavepacket. Assume it has an energy $E = E_F(1-\epsilon)$, $\epsilon \ll 1$. The WKB expressions for the transmittivity, normalised to the transmittivity at $E = E_F$, read

$$\frac{T_S(E_F(1-\epsilon))}{T_S(E_F)} = \exp(-\epsilon k_F s\sqrt{E_F/\phi}) \tag{3.7a}$$

and

$$\frac{T_T(E_F(1-\epsilon))}{T_T(E_F)} = \exp(-2\epsilon k_F s\sqrt{E_F/\phi}) \tag{3.7b}$$

where the subscripts 'S' and 'T' stand for square and triangular barriers respectively. From (3.7) it follows immediately that the triangular barrier is a much more effective

filter than the square barrier for plane waves with $E < E_F$. It should be stressed that from formulae (3.5) and (3.7*a*, *b*) the angular spread $\Delta\theta$ is approximately $(2\phi^{1/2}/E_F s)^{1/2}$ for a square barrier and $(\phi^{1/2}/E_F s)^{1/2}$ for a triangular one. Also at constant intensity the spread goes as $\phi^{1/2}$ in both cases. Therefore the *lower* the tunnel barrier height, the more focused the beam is, provided that the WKB approximation can be applied.

As pointed out above, 2D TDSE simulations of this kind require a lot of computer memory as we need to store the wavefunction and some intermediate data for all lattice points. From a physical point of view this constraint forces us to choose relatively small values of the width κ ($\kappa \leq 2$ in our 2D simulations) of the initial Gaussian packet. In practice $1 \leq \kappa \leq 2$, yielding an energy spread $\Delta E/E_F \simeq 10\%$. This is far away from the plane-wave regime ($\kappa \to \infty$).

To investigate the effect of the width κ on the properties of the transmitted wave, we have carried out very accurate simulations for 1D systems, for $\kappa \leq 40$. As a check a Gaussian packet having $\kappa = 40$ incident on a rectangular barrier of height $1.5E_F$ and width $d = 1.667$ was followed in time and analysed very carefully. The spread in energy of the $t = 0$ Gaussian packet $\Delta E = 0.0056E_F$, yielding a transmittivity $T = 0.155 \times 10^{-5}$ whereas the exact result for an incident plane wave of energy $E = E_F$ is $T = 0.132 \times 10^{-5}$. Thus, in spite of the fact that we are dealing with a rather large simulation box ($830\lambda_F$), on a quantitative level we are not yet close to the idealised plane-wave regime. However, detailed examination of the simulation data reveals that the functional dependence of a transmittivity for finite κ as a function of E fits extremely well to the well known expression for the transmission coefficient of a plane wave.

A direct consequence of working with wavepackets instead of plane waves is that each of the plane-wave constituents of the wavepacket tunnels through the potential barrier in a different manner. As a result, the mean energy and the spread in energy of the transmitted packet will be a function of the width κ of the initial packet. To investigate this aspect in more detail we have carried out simulations for incident Gaussian packets of various mean energies $E = \langle\psi(t = 0)|H|\psi(t = 0)\rangle$, and widths $\kappa = 4$, 20, 40 yielding energy spreads of $\Delta E/E_F \simeq 5$, 1, and 0.5% respectively. The probability amplitudes of the transmitted Fourier-transformed wavefunction were added, taking into account the corresponding transmittivities, and plotted as a function of E/E_F. The results are summarised in figure 17. Most striking is that the position of the maximum of the total transmittivity increases as the width κ decreases. For a wavepacket width of $0.05E_F$ the peak position shifts by about 5%. The reason for this behaviour is readily traced back to the tunnel characteristics of the barrier; the larger the energy of the plane-wave constituent, the larger its transmittivity.

4. Proposals for experiments

Our calculations suggest a set of experiments that could be performed to gain a better understanding of the focusing and coherence properties of the emitted beams. Such experiments might be done not only by using field emission from tips but also by other, physically very similar, techniques. For instance polarised light impinging on small orifices (pin holes) covered by a thin metal layer (playing the role of the tunnel barrier for electrons), or experiments such as those performed in 2D GaAs gas [11, 12] but having in addition a thin GaAlAs layer that will act as a tunnel barrier. We also discuss in more detail the consequences of the energy distribution of the

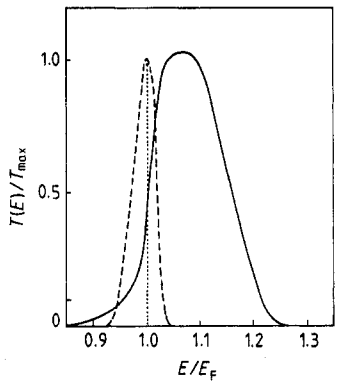

Figure 17. Normalised energy distribution of the total transmission probability, of a 1D triangular barrier of height $1.5E_F$ and base $5\lambda_F$. Full curve: $\Delta E/E_F = 5.6\%$; broken curve: $\Delta E/E_F = 1.1\%$; dotted curve: normalised transmission probability for a Gaussian packet having energy E_F and $\Delta E/E_F = 0.56\%$. TDSE calculation.

emitted electrons and how variations in it could be detected by increasing the applied potentiel or equivalently the emitted current. At the end some suggestions are made for performing electron interferometry and holography in the reflection mode

4.1. Energy distribution of the emitted electrons

In figure 5 we have presented the energy distribution of the emitted electrons at zero temperature, taking into account electrons very close to the Fermi surface only. For large currents this description is incomplete because electrons of energy slightly above or below the Fermi level will feel a different tunnel barrier and will contribute to the electron current also. This effect may increase to some extent the width of the energy distribution. This is illustrated in figure 18 where we present SDA calculations for the energy distribution for several temperatures of the emitting tip. However, increasing the temperature is not the only effect that has to be taken into account because in the SDA the electrons are still treated as monoenergetic plane waves, having energies at the Fermi level distributed according to the Fermi distribution of the metal. Increasing the current by increasing the applied field, the electrons in the metal will also experience more inelastic scattering and electron–electron interactions will contribute to the self-energy as well. These effects can be accounted for by describing an electron as a wavepacket with a certain energy width, as is done in TDSE calculations.

The results of our calculations, some of which are presented in figure 17, show that not only does the width of the distribution increase with the width of the incident wave but also that there is a shift of the peak position towards an energy above the Fermi level. Our calculations yield positive shifts by up to 10% of the Fermi energy. In other words the mean energy of the emitted electrons is larger than the Fermi energy. This is because electrons with energy above the Fermi level have a larger tunnel probability. We propose to perform an experiment in which the emitted current is steadily increased to obtain sufficiently large currents and to study the shift of the peak position in the energy distribution of the emitted electrons.

4.2. 2D GaAs electron gas

As mentioned in the introduction, recent experiments on the 2D GaAs electron gas [11, 12] having high mobility (or equivalently a large mean free path) have shown

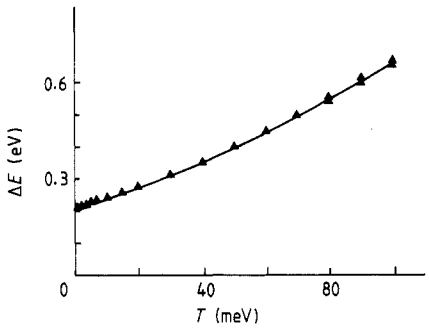

Figure 18. Energy spread as a function of temperature for a field $F = 0.5$ V Å^{-1}. SDA calculation.

that the conductance through constrictions of width W and length L (see figure 1 and figure 19(a)) is quantised as a function of W, the quantum of conductance being $G_0 = 1/R_0$, where $R_0 = h/2e^2 = 12900\Omega$. Each time that W increases by half a Fermi wavelength the conductance increases by G_0. In a first approximation (i.e. not self-consistently) this conductance has also been calculated and shows the same quantisation behaviour [13–18]. The same phenomena were suggested to occur in STM [20] and may have been observed in STM experiments [22]. However, in all these cases, on entering reservoir 2, the current density of the electrons going through the constriction is spread over approximately 60°, as shown in figure 4. The electron current is not focused.

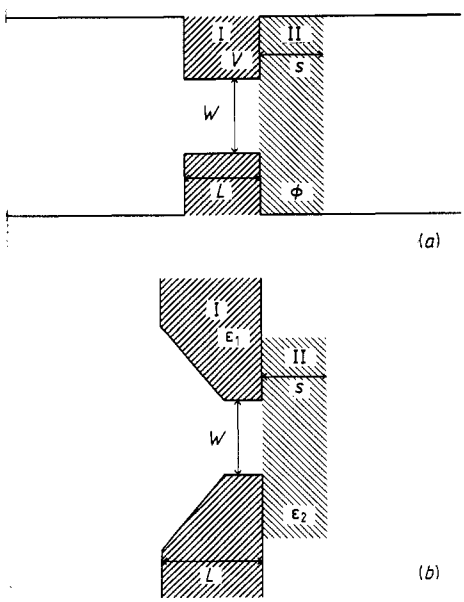

Figure 19. Geometry of the proposed GaAs device (a) and the optical experiment (b).

We believe that for technological applications it might be of interest to construct devices having focused electron currents so that by deflecting the current by a magnetic field one could direct the electrons to several different gates. To test these ideas we propose the following experiment. As shown in figure 19(a) two reservoirs having Fermi

wavelengths λ_1 and λ_2 are connected by a constriction, created by applying a positive potential V in the shaded area I of length L [11, 12]. This constriction quantises the conductance as a function of W but the current is not focused. We suggest two mechanisms to focus the current. One is to deposit a region II (see figure 19(*a*)) of GaAlAs having a thickness s and with a tunnel barrier height ϕ. Clearly this is nothing but the tunnel barrier of the field emission model discussed above and consequently focusing of the electrons from 60° to 10° will also occur, although it will be only partially because of the rectangular tunnel barrier. However, in the field emission case there is an additional mechanism to focus the electrons, namely the external applied field. This could be mimicked in the GaAs case too by applying a potential between reservoirs 1 and 2.

In field emission the beam propagates in vacuum but now the current propagates in a GaAs crystal. Another way to generate the applied field is to increase the doping in reservoir 2, i.e. by increasing the Fermi energy or reducing λ_2. It is worth noting that in the presence of a tunnel barrier in a device like that of figure 19(*a*), there is no quantisation of the conductance because only the lower bands of the constriction contribute to the current, whereas the other bands do not add significantly to the total current (see figure 5 for the field emission case). In figure 20 we present the outcome of some model calculations for the system described above. For curve A we have chosen $\lambda_1 = \lambda_2 = 335$ Å, a Fermi energy $E_F = 20$ meV, $\phi = 20$ meV corresponding to a tunnel distance of 53 Å, an $Al_xGa_{1-x}As$ layer of thickness $s = 371$ Å and $x = 0.06$. We have taken into account that the effective mass of the electron is that in GaAs, equal to 0.067, the bare electron mass. Curve B is obtained from a similar calculation but instead of $\lambda_2 = 335$ Å, we have taken $\lambda_2 = 167$ Å. For comparison the results for $\phi = 0$, i.e. without a tunnel barrier, are also shown. To illustrate the effect of the thickness of the tunnel barrier, figure 20 curve C depicts the results of a calculation for the same parameters as for curve B but for a thicker barrier (530 Å) which is approximately 1.5 times the wavelength of the electrons in reservoir 1.

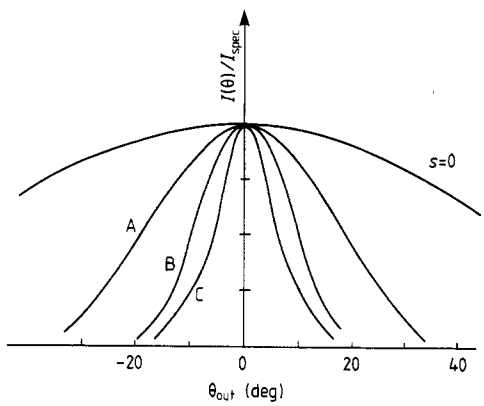

Figure 20. Angular distribution for the $Al_xGa_{1-x}As$ device depicted in figure 19(*a*), in the case without a barrier; (A) for $\lambda_1 = \lambda_2 = 335$ Å; (B) for $\lambda_1 = 335$ Å and $\lambda_2 = 167$ Å; (C) for the same wavelengths as in (B) but for a thicker barrier.

Our calculations clearly demonstrate that the method we propose is quite efficient in focusing the beam. This focusing effect should be stronger the lower the tunnel barrier is, the thicker the GaAlAs deposit is and the smaller λ_2 is. Having obtained

a focused electron beam, it should be possible to apply a magnetic field [28], and to direct the beam to specific areas in reservoir 2.

4.3. Light experiments

Scattering of polarised light passing through a small hole is also an appealing and very direct way to confront with experiments our ideas on the focusing of waves. In particular, the optical analogue of the point source may also be more convenient to study as an incident, coherent and monoenergetic beam of photons can be produced by a laser. Compared to electron waves, photons have the additional advantage that the experiment can be done with waves of well defined energy and angle of incidence whereas for electrons, one has to take into account contributions to the current of each electron at the Fermi level. Thus the light experiment would provide direct information about the diffraction properties for each angle of incidence separately.

Schematically this experiment is depicted in figure 19(*b*). Now the wavelengths of the incident (λ_1) and transmitted (λ_2) light are of course equal to the wavelength of light in vacuum. Region I is a metal pin hole having a diameter $W \simeq \lambda$, thickness L and a dielectric constant ϵ_1. Such pin holes are commercially available. Region II is another metal sheet of thickness s and dielectric constant ϵ_2, put on top of the pin hole. The choice of the two metals I and II should be such that their dielectric constant has a small imaginary part to avoid absorption of radiation by inelastic processes. On the other hand the real part of the dielectric constant should be large and negative so that tunnelling is effective. A good candidate might be Ag [29, 30], but care should be taken to avoid surface plasmon effects by properly choosing the angle of incidence and wavelength of the light. The roughness of the surface should be kept as small as possible in order to miminise the coupling of light with surface plasmons. In this respect Ag is very convenient because after annealing it is very flat.

Some model calculations have been performed for incident light of $\lambda = 5145$ Å, corresponding to a green Ar line. Following the suggestion made above, the material chosen for both regions I and II is Ag, so that for $\lambda = 5145$ Å the experimental value for the dielectric function $\epsilon_1 = \epsilon_2 = -11 + 0.33\mathrm{i}$ at $\lambda = 5145$Å [29]. The thickness L of the pin hole should be large enough that the amount of light not going through the hole is negligible. Note that in this model calculation, an Ag pin hole was taken but it is clear that for the actual experiment this is not essential. On the other hand, the thickness s of the region II should not be too large, as there should be a detectable amount of light in region II. The fact that one can detect very weak light intensities might be an additional advantage of working with light instead of electrons.

Some results for the diffraction pattern of the transmitted light are presented in figure 21 for incident angles of 0 and 28°. The data are normalised with respect to the value at the specular angle and should be compared to the diffraction patterns for $s = 0$, i.e. the case without a tunnel barrier. It is clearly seen that the angular distribution becomes narrower when the tunnel barrier is present. In addition, for $s > 0$ the diffraction profile is highly asymmetric.

4.4. Interferometry and holography in the reflection mode

It is clear that important applications of focused and coherent beams are to be found in electron microscopy at low energies. As discussed in earlier work [4, 5] and in this work, electron beams produced by atomic-size sources have transverse coherent lengths of the order of millimetres to a centimetre. This is approximately three orders of magnitude

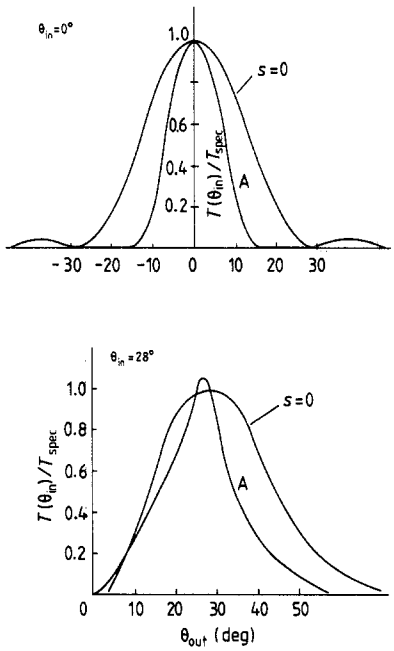

Figure 21. Calculated angular distribution for the light experiment of which the geometry is shown in figure 19(*b*). Curve A is the result for $s \simeq 300$ Å.

larger that those obtained with normal field-emission tips [4, 5, 8]. Estimating the brightness of the beams produced by these small sources one finds [4] that it can be made 10^4 to 10^6 larger than for usual field-emission sources. This implies an increase in the number of detectable interference fringes of 10^2 to 10^3 [8–10]. In addition the energy of these beams is in the range of 100 to 1000 V.

Given these characteristics, such electron sources should be more than adequate for performing electron interferometry and holography in the reflection mode. Interferometry and holography as proposed by Gabor [6, 7] has been performed with electrons in the region of 100 000 V working in the transmission mode [8, 9], i.e. with a thin sample and the electrons that go through it. As the electron sees a rapidly changing environment when it passes through the sample, information contained in the electron wavefunction phase is averaged out and is therefore partially lost. Consequently holograms obtained by this technique have high (atomic) resolution in the direction transverse to the beam but very poor resolution, from the atomic point of view, in the longitudinal direction [8, 9]. The electrons beams generated by very small sources have much smaller energies and therefore their penetration depth in the sample is smaller. We propose to perform interferometry and holography in the reflection mode because then the electron will not penetrate into the sample as much and consequently the averaging process may be negligible. Given the high degree of brightness and coherence of the beam it might be possible to achieve three-dimensional atomic resolution [4]. Similar results could be obtained qualitatively from low-energy electron diffraction, by considering the diffraction intensity of a hologram from two different electron paths.

5. Conclusions

Our calculations have shown very clearly that of all geometries studied, the combination of a plane emitting surface and a triangular barrier yields the best focusing of the emitted electron beam. For a work function $\phi = 4.5$ eV, and currents of 10^6 to 10^9 A cm^{-2} corresponding to fields of 0.5 and 1 V Å^{-1}, the angular spread at the screen is estimated to be 2 and 3° respectively. Of course for a given current the focusing will be better if ϕ is smaller. If the equipotential line for E_F at the apex of the tip is flat, the emitted beam will be focused according to our calculations. We conjecture that this is what causes the focusing of electrons emitted from microtips. The presence of quantised levels in the tip does not seem to affect the focusing properties.

Acknowledgments

We deeply appreciate extensive interactions with Dr H Rohrer. We wish to thank Dr V T Binh for many helpful and stimulating discussions and L Escapa for her active participation and help with computations. We also want to thank IBM Research Laboratories Zürich for kind hospitality.

The work of NG and JJS is partially supported by a joint agreement between the Universidad Autónoma de Madrid and IBM Research Laboratories, Zürich. HDR would like to thank the Control Data Corporation (The Netherlands) for a generous grant of computer time on the CYBER 205, the University of Leuven for providing unrestricted access to their IBM 3090-300/VF, and the Belgian National Science Foundation for financial support.

References

[1] Fink H-W 1986 *IBM J. Res. Dev.* **30** 460
[2] Fink H-W 1988 *Phys. Scr.* **38** 260
[3] Vu Thien Binh and Marieu J 1988 *Surf. Sci.* **102** L539
[4] García N and Rohrer H 1989 *J. Phys.: Condens. Matter* **1** 3737
[5] Serena P, Escapa L, Sáenz J J, García N and Rohrer H 1989 *J. Microsc.* **152** 43
[6] Gabor D 1949 *Proc. R. Soc.* A **454** 197
[7] Gabor D 1951 *Proc. R. Soc.* B **64** 449
[8] Tonomura A 1987 *Rev. Mod. Phys* **59** 639
[9] Lichte H 1986 *Ultramicroscopy* **20** 293
[10] Missiroli F G, Pozzi G and Valdre U 1981 *J. Phys. E: Sci. Instrum.* **14** 649
[11] van Wees B J *et al* 1988 *Phys. Rev. Lett.* **60** 848
[12] Wharam D A, Thornton T J, Newbury R, Pepper M, Ahmed H, Frost J E F, Hasko D G, Peacock D C, Richie D A and Jones G A C 1988 *J. Phys. C: Solid State Phys.* **21** L209
[13] García N and Escapa L 1989 *Appl. Phys. Lett.* **54** 1418
[14] Escapa L and García N 1989 *J. Phys. C: Solid State Phys.* **1** 2125
[15] Kramer B and Mašek J 1989 *J. Phys. C: Solid State Phys.* **21** L1147
[16] Szafer A and Stone D 1989 *Phys. Rev. Lett.* **62** 300
[17] Kirkzenow G 1989 *Solid State Commun.* **68** 715
[18] Haanappel E G and van der Marel D 1989 *Phys. Rev.* B **39** 5484
[19] García N and Escapa L 1989 *Appl. Phys. Lett.* at press; 1990 *Proc. NATO Meeting Basic Concepts and Applications of Scanning Tunnelling Microscopy (STM) and Related Techniques (Erice, 1989)* (Amsterdam: Kluwer) to be published
[20] García N 1987 *Oscillatory Behaviour in the Quantum Elastic Resistance of Small Contacts* Talk at STM Workshop, Trieste, July 1987

[21] Binnig G and Rohrer H 1986 *IBM J. Res. Dev.* **30** 355
[22] Gimzewski J K and Moller R 1987 *Phys. Rev.* B **36** 1284
[23] García N, Ocal C and Flores F 1983 *Phys. Rev. Lett.* **50** 2002
[24] Stoll E, Selloni A and Carnevali P 1984 *J. Phys. C: Solid State Phys.* **17** 3073
[25] García and Stoll E 1988 *Phys. Rev. Lett.* **37** 445
[26] De Raedt H 1987 *Comput. Phys. Rep.* **7** 1
[27] Schiff L I 1968 *Quantum Mechanics* (New York: McGraw–Hill)
[28] van Houten H, van Wees B J, Mooij J E, Beenakker C W J, Williamson J G and Foxon C T 1988 *Europhys. Lett.* **5** 721
[29] Johnson P B and Christy R 1972 *Phys. Rev.* B **6** 4370
[30] García 1983 *Opt. Commun.* **45** 307